INFLUENCE OF PROPELLER PRESENCE AND CAVITATION ON LIQUID NUCLEI POPULATION

Reni Raju
DYNAFLOW INC.
Jessup, MD - 20794
reni@dynaflow-inc.com

Chao-Tsung Hsiao
DYNAFLOW INC.
Jessup, MD - 20794
ctsung@dynaflow-inc.com

Georges Chahine
DYNAFLOW INC.
Jessup, MD - 20794
glchahine@dynaflow-inc.com

ABSTRACT

The modification of the bubble nuclei population due to the presence of a rotating propeller was modeled numerically using a combined Eulerian - Lagrangian approach. The liquid flow field was solved using a Reynolds Averaged Navier-Stokes (RANS) solver and was improved further using Direct Navier-Stokes Simulations (DNSS) to better capture the wake rollup in the tip-vortex. Bubbles were propagated in the resulting flow field using a Lagrangian approach and computing bubble motion and volume change. Resulting nuclei distribution modification downstream of the propeller for various advance coefficients was studied. The results show that different advance coefficients can result in very different cavitation zones near the propeller as the cavitation number is reduced below the cavitation inception limit. This has a strong effect on the nuclei population downstream of the propeller.

We further examine the effect of non-uniformity in the upstream distribution of nuclei, and the effects of gravity and propeller scale on the results. Increasing the scale appears to play a major role in increasing the void fraction downstream.

INTRODUCTION

The presence of bubbles in the wake of a ship can be a safety concern due to the high acoustic response of bubbles to acoustic waves from homing devices. These bubbles, commonly thought to be generated at the free surface, are generally transported by the flow field to the stern area, captured in the ship wake, trapped in the large vortical structures and hence act as tracers of the ship wake. Previous investigations in this area have primarily focused on bubble entrainment in breaking waves [1][2][3], while little focus has been paid on the other means of bubble generation/entrainment. One of the potential sources of bubble generation in the ship wake is due to the entrainment by the ship propellers. The presence of bubbles can be attributed to the fundamental observation that any water contains microscopic sub-visual bubble nuclei that act as seeds for many phenomena in mechanical and chemical engineering such as: cavitation, boiling, gas transfer, chemical reactions, etc. On encountering propeller cavitation the nuclei eventually undergo local explosive growth, collapse and oscillations causing cumulative gas transfer into the bubbles.

To investigate bubble production by the propeller, we have developed a computational tool to predict bubble size and void fraction distribution downstream of the propeller. In our previous studies [4] we have identified that gas diffusion plays an important role on the bubble dynamics in this problem. The bubble size downstream of the propeller is larger than the original upstream size due to a net influx of dissolved gas into the bubble. The previous studies were based on a RANS solution of the flow generated by the propeller. However, RANS solutions are now known to be inadequate for predicting the tip vortex flow accurately [5][6][7]. Hsiao and Chahine [8][9] have found that the RANS solution of the tip vortex flow can be significantly improved by conducting Direct Navier-Stokes Simulation (DNSS or Implicit LES) in a reduced computational domain surrounding the tip vortex line. This combined RANS-DNSS is used in the current study to predict bubble entrainment downstream of the propeller.

It our previous studies, we have found that bubble explosive growth and collapse, are an essential 'catalyst' to enable significant diffusion. Therefore, one of the primary parameters determining the intensity of the growth and collapse of the bubble is the cavitation number. On the other hand the cavitation type and the locations of the cavitation regions may be different when the propeller is operated under different advance coefficients. The effect of cavitation number has been previously presented in [4] and hence in the current study we investigate the effect of the advance coefficient on nuclei population modification.

In addition to the parameters affecting cavitation, the downstream bubble population obviously depends on the initial upstream bubble size distribution. The presence of a ship hull can lead to non-uniform spatial distribution of the bubbles and

hence the effect of such distribution was also explored. In order to improve the model prediction further the effect of gravity and propeller scale was also studied.

NUMERICAL METHODOLOGY

Flow Solver for RANS Computation

In order to model the propeller flow field the flow was obtained by solving the unsteady Navier-Stokes equations in the rotating frame given in non-dimensional notation as,

$$\nabla \cdot \mathbf{u} = 0 , \tag{1}$$

$$\frac{D\mathbf{u}}{\partial t} = -\nabla p + \frac{1}{R_e}\nabla^2 \mathbf{u} + \Omega^2 \mathbf{r} - 2\Omega \times \mathbf{u} , \tag{2}$$

where the latter two terms in Eqn. (2) are the centrifugal force and the Coriolis force terms respectively.

To solve Equations (1) and (2) numerically, a three-dimensional incompressible Navier-Stokes solver, INS3D, developed by Rogers et al. [10], was applied to compute the RANS solution of the rotating propeller flow in the rotating frame of reference with the Baldwin-Barth one equation model.

Flow Solver for DNSS Computations

For the reduced domain DNSS calculations described later, Equations (1) and (2) are solved using DYNAFLOW's flow solver 3DYNAFS-VIS. 3DYNAFS-VIS has evolved from its previous version, DF_UNCLE, and now includes the viscoelastic model for simulation of non-Newtonian polymer solution flow, an Eulerian/Lagrangian two-way coupling scheme for simulation of bubble/liquid two phase flows and a Level Set method for simulation of large-deformation free surface flows.

3DYNAFS-VIS is based on the artificial-compressibility method [11], in which an artificial time derivative of the pressure is added to the continuity equation as

$$\frac{1}{\beta_c}\frac{\partial p}{\partial t} + \nabla \bullet \mathbf{u} = 0 , \tag{3}$$

where β_c is an artificial compressibility factor. As a consequence, a hyperbolic system of equations (1) and (2) and is formed and is solved using a time marching scheme in the pseudo-time to reach a steady-state solution. To obtain a time-dependent solution, a Newton iterative procedure is performed in each physical time step in order to satisfy the continuity equation.

The numerical scheme in 3DYNAFS-VIS uses a finite volume formulation. A first-order Euler implicit difference formula is applied to the time derivatives. The spatial differencing of the convective terms uses the flux-difference splitting scheme based on Roe's method [12]and a van Leer's MUSCL method for obtaining the first- or third-order fluxes. A second-order central differencing is used for the viscous terms which are simplified using the thin-layer approximation. The flux Jacobians required in an implicit scheme are obtained numerically. The resulting system of algebraic equations is solved using a discretized Newton Relaxation method in which

symmetric block Gauss-Seidel sub-iterations are performed before the solution is updated at each Newton interaction.

Bubble Dynamics Model

To model nuclei dynamics in the propeller flow, a multi-bubble dynamics and trajectory code, DF_MULTI_SAP$^©$, was applied to track the bubble nuclei and predict their acoustic signals during cavitation events. In DF_MULTI_SAP$^©$ the bubble transport is modeled via the motion equation described by Johnson & Hsieh [14], while the bubble dynamics is simulated by solving a Surface Averaged Pressure (SAP) Rayleigh-Plesset equation [15].

In the present study we have considered the following form of the equation for the bubble radius, $R(t)$, which accounts for liquid and gas compressibility, liquid viscosity, surface tension, and non-uniform pressure fields, and is based on Gilmore's approach [16].

$$(1-\frac{\dot{R}}{c})R\ddot{R} + \frac{3}{2}(1-\frac{\dot{R}}{3c})\dot{R} = \frac{\left(\mathbf{u}_{enc} - \mathbf{u}_b\right)^2}{4}$$
$$+ \frac{1}{\rho}(1+\frac{\dot{R}}{c}+\frac{R}{c}\frac{d}{dt})\left[p_v + p_g - p_{enc} - \frac{2\gamma}{R} - 4\mu\frac{\dot{R}}{R}\right] \tag{4}$$

where c is the sound speed, ρ is liquid density, p_v is the vapor pressure, p_g is the gas pressure, γ is the surface tension and μ is the viscosity. In Equation (4), which we have dubbed the Surface-Averaged Pressure (SAP) bubble dynamics equation [15], we have accounted for a slip velocity between the bubble and the host liquid, and for a non-uniform pressure field along the bubble surface. p_{enc} and $\mathbf{u}_{enc}$ are defined as the average of the liquid pressures and velocities over the bubble surface. The use of p_{enc} results in a major improvement over the classical spherical bubble model which uses the pressure at the bubble center in its absence. The gas pressure, p_g, is obtained, as described in the next section, from the solution of the gas diffusion problem and the assumption that the gas is an ideal gas. The bubble trajectory is obtained using the following motion equation [14]:

$$\frac{d\mathbf{u}_b}{dt} = -\frac{3}{\rho}\nabla P - 2g + \frac{3}{4}\frac{C_D}{R}\left(\mathbf{u}_{enc} - \mathbf{u}_b\right)\left|\mathbf{u}_{enc} - \mathbf{u}_b\right|$$
$$+ \frac{3}{2\pi}\frac{C_L}{R}\sqrt{\frac{\mu}{\rho}}\frac{\left(\mathbf{u}_{enc} - \mathbf{u}_b\right)\times\boldsymbol{\omega}}{\sqrt{|\boldsymbol{\omega}|}} + \frac{3}{R}\left(\mathbf{u}_{enc} - \mathbf{u}_b\right)\dot{R}, \tag{5}$$

where $\mathbf{u}_b$ is the bubble velocity, g is gravity, C_L is the lift coefficient, $\boldsymbol{\omega}$ is vorticity, and C_D is the drag coefficient given by an empirical equation such as that of Haberman & Morton [17]:

$$C_D = \frac{24}{R_{eb}}\left(1 + 0.197R_{eb}^{0.63} + 2.6\times10^{-4}R_{eb}^{1.38}\right),$$

$$R_{eb} = \frac{2\rho R\left|\mathbf{u}_{enc} - \mathbf{u}_b\right|}{\mu}. \tag{6}$$

The last term on the right hand side of Eqn. (6) is the force due to the bubble volume variations, which is obtained by solving Equation (4).

Gas Diffusion Model

Water can contain gas not only in the form of nuclei with a particular distribution, but also as dissolved gas with a concentration C. In the presence of a local concentration gradient, dissolved gas will diffuse from the high concentration to the low concentration region. The transport equation for the time and space dependent dissolved gas concentration, C, in the liquid is given by:

$$\frac{\partial C}{\partial t} + \mathbf{u} \cdot \nabla C = D_g \nabla^2 C, \tag{7}$$

where D_g is the molar diffusivity of the gaseous component in the liquid (in practice the turbulent diffusivity is also used in high turbulence areas). Concerning bubble dynamics, the following initial and far field boundary conditions apply:

$$\begin{aligned} C &= C_\infty \quad \text{for } t = t_0, \\ C &\to C_\infty \quad \text{for } r \to \infty, \end{aligned} \tag{8}$$

where r is the distance from the bubble center and C_∞ is the dissolved gas concentration far away from the bubble surface.

The conditions at the bubble interface are very important and actually drive the gas diffusion. The first condition states that the gas concentration in the liquid at the interface is the saturation gas concentration:

$$C = C_s \quad \text{at } r = R, \tag{9}$$

where C_s is the dissolved gas concentration at the bubble surface on the liquid side. The saturation concentration is connected to the partial gas pressure, p_g, through Henry's law:

$$p_g = H C_s, \tag{10}$$

where H is the Henry constant.

In addition, we write an equation of gas transfer at the bubble/liquid interface:

$$D_g \int_S \frac{\partial C}{\partial n} dS = \dot{n}_g. \tag{11}$$

This equation directly connects the diffusion of gas at the interface with the interfacial area and the transfer rate of gas moles, $\dot{n}_g$, between the liquid and the bubble.

Since numerical solution of Equation (7) requires gridding of the full space, Plesset and Zwick[19] introduced a very useful approximation in the case where the changes in gas concentration are restricted to a boundary layer around the bubble. An analytical solution then exists and relates the gas concentration at the bubble wall to the concentration at "infinity". This expression requires integration over the whole history of the bubble dynamics in order to enable computation of the amount of gas exchange at the bubble wall, and has the following form:

$$C_s = C_\infty - \frac{1}{4\pi\sqrt{\pi D_g}} \int_0^t \frac{\dot{n}_g}{\left[\int_\tau^t R^4(y) dy \right]^{1/2}} d\tau. \tag{12}$$

One should note that to solve the bubble volume Equation (4) we need the gas pressure, p_g, and to get p_g we need the history of the variations of the bubble radius and the rate of transfer of gas moles, $\dot{n}_g$, across the bubble interface.

The problem is closed by considering the thermodynamics of the contents of the bubble. The two components of the bubble content: vapor and gas, are both assumed to be ideal gases which follow an ideal gas law:

$$\begin{aligned} p_g V_b &= n_g R_u T_b; \qquad p_v V_b = n_v R_u T_b, \\ n_v &= n_g (p_v / p_g). \end{aligned} \tag{13}$$

One consequence of this assumption is that the amount of gas, n_g, and vapor, n_v, in the bubble are directly proportional to the ratio of their respective partial pressures. Since these quantities change in time because of both mass exchange and compression/expansion, we consider their dynamics through the thermodynamics inside the bubble and energy balance on the bubble control volume.

$$dU = -dW + \sum_{i=v,g} \dot{n}_i \, h_i \, dt, \tag{14}$$

where

$dU = \sum_{i=v,g} c_{v,i} \, d(n_i T_i)$ is change in internal energy,

$dW = (p_v + p_g) \, dV_b$ is work done by control volume,

$h_i = \sum_{i=v,g} \dot{n}_i \, c_{p,i} \, T_l$ is specific enthalpy.

Chahine et al.[20][21] reduced the equations of determining p_g to the following two differential equations:

$$\dot{p}_g = \frac{E/p_g - D p_g - F}{A + B/p_g^2}, \tag{15}$$

with $A, B, D, E, F = f\left(R, \dot{R}, n_g, \dot{n}_g\right)$

$$\dot{n}_g(t) = \frac{R^2}{2\sqrt{h}} \left[\frac{C_\infty - \dfrac{P_g}{H}}{\dfrac{1}{4\pi\sqrt{\pi D_g}}} - \int_0^{t-h} \frac{\dot{n}_g}{\left[\int_\tau^{t-h} R^4(y) dy \right]^{1/2}} d\tau \right]. \tag{16}$$

To determine each bubble motion and volume variations, the set of four differential Equations(4), (5), (15), and (16) were solved using a Runge-Kutta fourth-order scheme to integrate through time.

RANS-DNSS Approach

For the current study the open five-blade DTMB Propeller 5168 with a 15.86 inch diameter is considered. The flow field around this propeller has been extensively studied previously [6][7]. Following the work of Hsiao and Pauley[6] an H-H type was used to construct a single passage blade configuration with 2.4 million grid points for the RANS calculations. Periodic

boundary conditions were used on both the suction and pressure sides. The grid follows the incoming flow angle forming a spiral domain, seen in Figure 1, with the inflow located at 1.8R and the outflow at 2R from the propeller mid-plane. The computational domain extends 2R from the hub which is represented as a solid wall in the simulations. Care was taken to ensure that the grid point closest to the rigid boundary was located at distance of $y^+ \sim 2$ from the grid surface.

In order to overcome the deficiency of RANS computations in predicting the tip vortex region accurately, a reduced computational domain was constructed using the block grids shown in Figure 1. The domain was constructed using 7-blocks around the tip vortex centerline region extending from the blade tip to the end of the original domain. The original RANS solution is interpolated onto the $245 \times 121 \times 121$ grid and serves as the initial condition to the DNSS solver.
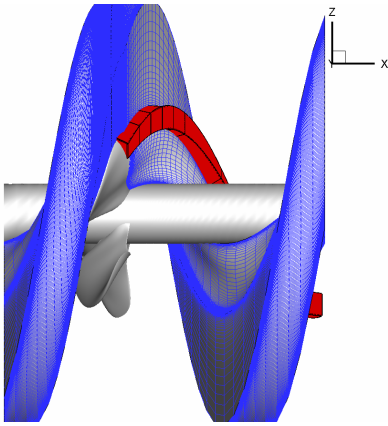
Figure 1. Computational H-H and 7-block grids used for RANS and DNSS simulation respectively.

RESULTS AND DISCUSSION

### Bubble Entrainment in the Propeller Flow Field

Due to their averaging nature, the RANS computations although able to capture the initial tip vortex roll up, are unable to resolve correctly the development of the viscous core further downstream. This shortcoming can be overcome by improving the resolution and not applying a turbulence model in the region of interest. To illustrate this, Figure 2 shows the streamwise vorticity contours for an advance coefficient, $J = 1.1$ and a Reynolds number, $R_e = 4.19 \times 10^6$. The corresponding freestream velocity is $U_\infty = 10.7$ m/s and propeller rotational speed is $n = 1450$ rpm. Figure 2 shows the contours on grid planes perpendicular to the vortex trajectory for both RANS and DNSS solutions. It is seen that the interaction between the tip vortex and the blade wake (vortex sheet) is much weaker in the RANS solution due to excessive vortex diffusion and dissipation. On the other hand, in the combined RANS/DNSS solution, the tip vortex is seen to preserve its strength as the vortex sheet continuously rolls up into the tip vortex. As a

result of a stronger vortex rollup, a greater pressure drop is observed, which influences the bubble dynamics directly.

To study the nuclei population modification in the propeller flow field, a set of nuclei with a given bubble size distribution were released upstream of the computational domain. The subsequent bubble behavior was tracked and a time-averaged void fraction deduced once the number of the bubble within the computational domain reaches a steady state. The detailed description of the computations of the time-averaged void fraction can be found in [4].
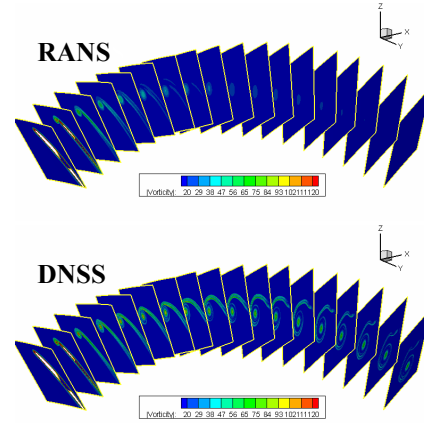

Figure 2: Comparison of vorticity contour for solutions obtained by RANS and DNSS for $J = 1.1$.
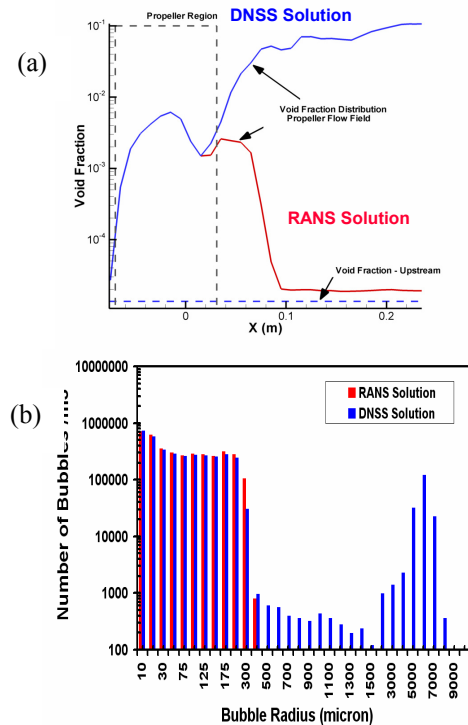
Figure 3: Comparison of (a) time-averaged void fraction variation along x, and (b) bubble size distribution at $x = 0.2$m for RANS and DNSS solutions $J = 1.1$ and $\sigma = 1.75$.

Figure 3 shows a comparison of the time-averaged void fraction and downstream nuclei size distribution obtained with the RANS and RANS/DNSS solutions for a cavitation number of $\sigma= 1.75$ and an initial bubble size distribution 10-300 μm. It is seen that the void fraction is significantly increased downstream of the propeller for the more accurate DNSS solution. The DNSS solution leads to a wider and larger bubble size distribution downstream as compared to the RANS.

(a)

(b)
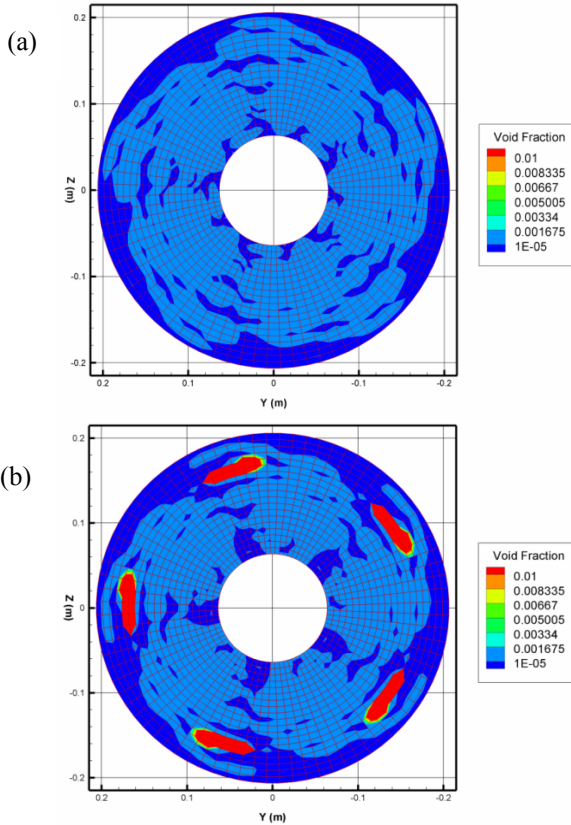
Figure 4: Comparison of time-averaged void fractions at a distance of x = 0.22 m from the leading edge of the propeller.

Figure 4 compares the time-averaged void fraction contours for both RANS and DNSS solutions at a downstream location x=0.22 m. It is seen that the high void fraction areas are concentrated in the tip vortex region for both cases. However, the high concentration area is much more extensive for the DNSS solution.

Effect of Advance Coefficient

As demonstrated in the previous section, use of DNSS can lead to a significant improvement in the tip vortex solution. The results of studies presented henceforth are based on using this approach unless specified otherwise. The effect of the advance coefficients on the results was studied for two advance coefficients, $J = 1.1$ and 1.27. For $J = 1.27$, the corresponding parameters are R_e=3.88 × 10^6, U_∞= 11.08 m/s and n = 1,300 rpm.

(a)

(b)
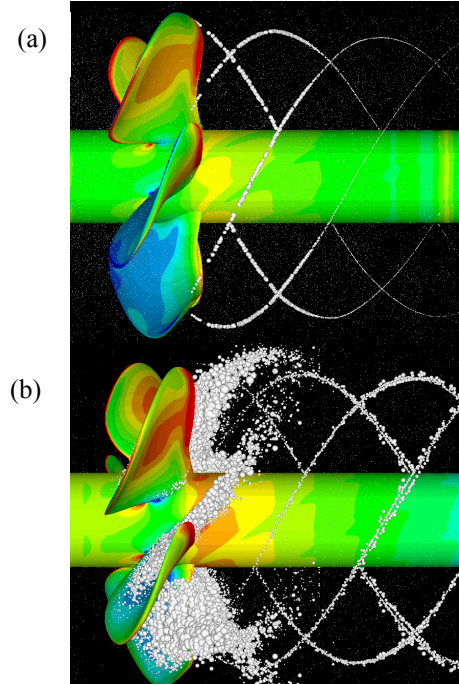
Figure 5. Comparison of Nuclei distribution in the flow field for (a) J=1.1 at σ=2.75 and (b) J=1.27at σ=1.0.
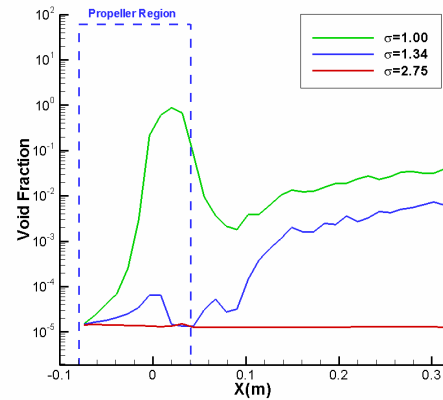

Figure 6. Comparison of the time-averaged void fractions vs. distance for J=1.27 at different cavitation numbers.

Figure 5 shows the nuclei distribution in the flow field for $J = 1.1$ at $\sigma = 2.75$ and $J = 1.27$ at $\sigma= 1.0$. We can see that different advance coefficients can result in very different cavitation zones near the propeller as the cavitation number is reduced below the inception number. For $J = 1.1$ the cavitation is already fully developed in the tip vortex at $\sigma = 2.75$ while no cavitation is observed on the blade surface. For $J = 1.27$ a much lower cavitation number is required to have the cavitation start to appear in the flow field. At sufficiently low cavitation numbers, cavitation was observed both on the blade and in the tip vortex. Figure 6 shows the resulting void fractions versus distance for three different cavitation numbers for the advance coefficient, $J = 1.27$. It is seen that as the cavitation number

increases the downstream void fraction decreases. At low cavitation numbers cavitation occurs not only in the tip vortex region but also on the propeller blade for $J = 1.27$.

The change in the locations of cavitation occurrence also results in very different high void fraction distributions downstream of the propeller as shown in Figure 7. We observe that the high void fraction concentration is only in the tip vortex region for $J = 1.1$ at $\sigma = 2.75$ while it is observed in both the tip vortex and the wake regions of the blades for $J = 1.27$ at $\sigma = 1.0$.
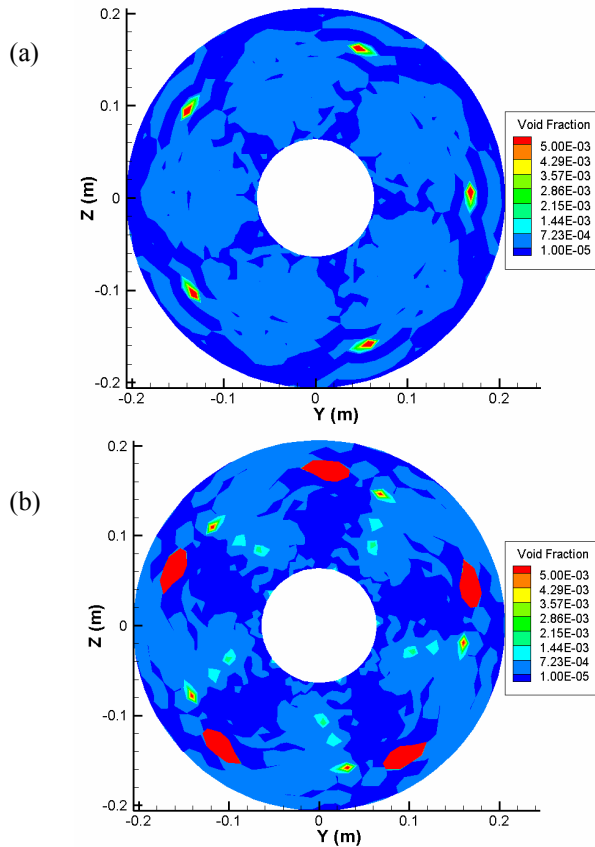

Figure 7. Comparison of the downstream void fraction contours in the x=0.22m plane for (a) J=1.1 at σ=2.75, and (b) J=1.27at σ=1.0.

### Effect of Non-Uniform Bubble Distribution

In practical conditions, the flow field entering the propeller disk can be significantly affected by the presence of the ship hull. The nuclei which are entrained along the ship hull and swept down to the stern region can also result in a non-uniform bubbly flow into the propeller. We studied this aspect of the problem for the baseline case of $J = 1.1$ and $\sigma = 2.75$. A bubble size distribution of 30-200 μm was chosen for three different configurations as shown in Figure 8. In the uniform distribution condition, the bubbles are distributed randomly in the release plane in a uniform manner. On the other hand stratified distributions were obtained as weighted distributions in the

vertical direction with a larger number of bubbles at shallower depths. Two stratified distributions were selected, one with bubbles linearly distributed across one diameter of the propeller from 0 to 1 and the second one with bubbles only in the upper 0.75 diameter as seen in Figure 8(b) and (c) respectively. In order to account for this non-uniform distribution in the rotating frame of reference, the upstream nuclei were released in a predetermined spiral domain. The distribution of nuclei was such that a given location in the x-direction corresponded to the correct phase of rotation of the propeller. While keeping the bubble distribution random in space with the desired size distribution, this biased it to produce the desired z stratification.
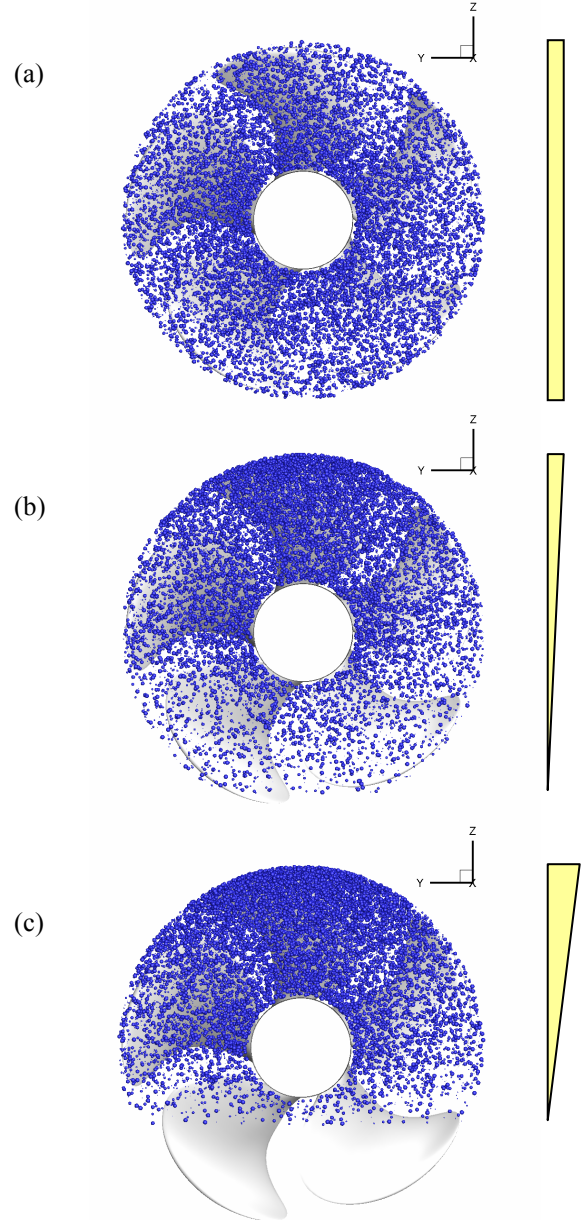
Figure 8. Upstream bubble (a) uniform distribution and stratified distribution in (b) 1D and (c) 0.75D.
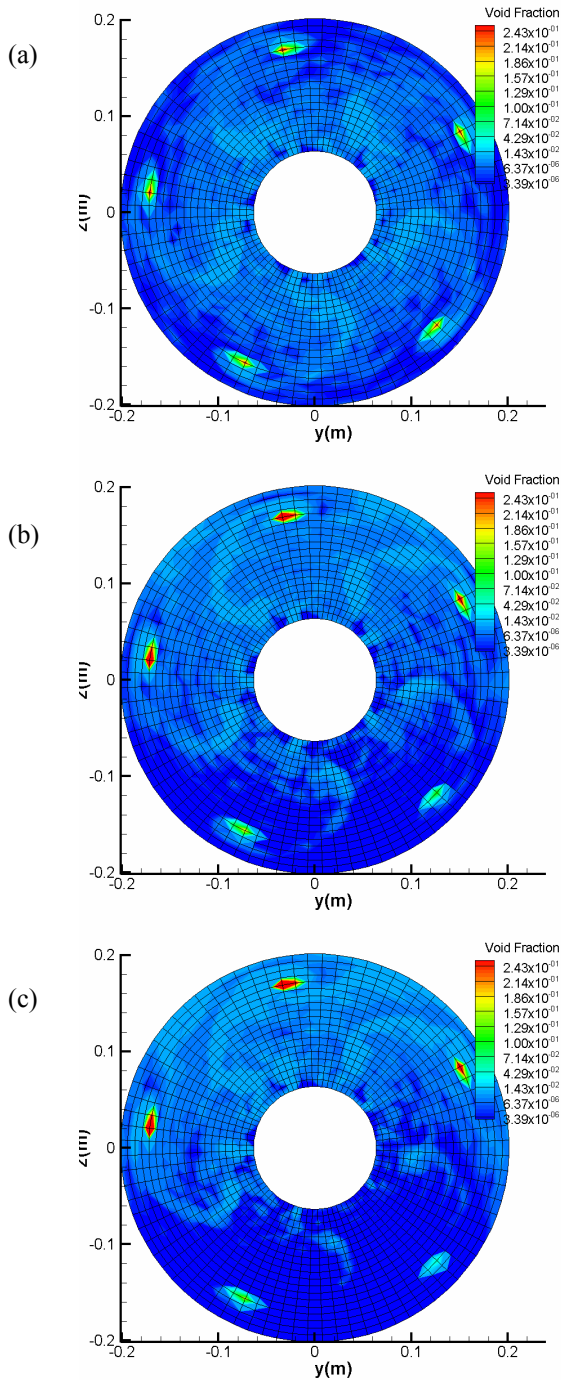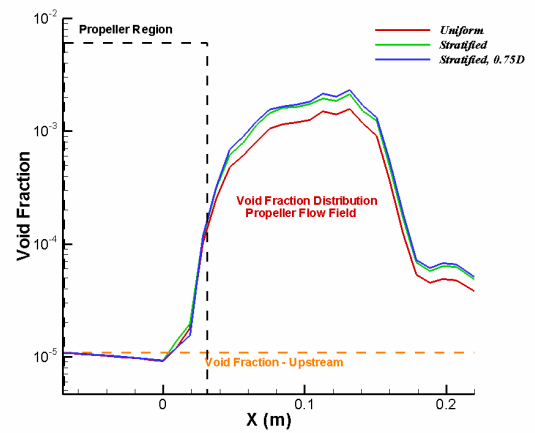
Figure 9. Time-averaged void fraction contours at x=0.13 m (a) uniform distribution and stratified distribution in (b) 1D and (c) 0.75D.

Figure 9 shows the void fraction distribution at x=0.13m for all three cases. It is seen that the stratification significantly affects the void fraction distribution downstream of the propeller. For the uniform upstream distribution the void fraction shows an equally high concentration in the tip vortex regions for all the five blades, while the upper tip vortices have higher void fraction in comparison to the ones near the bottom in the stratified cases. Distribution of the bubbles in the rest of the flow field also show a clear effect of stratification.

Figure 10 compares the time-averaged void fractions along the x-direction for the three cases. Although both stratified cases give a comparable void fraction, the uniform distribution yields nearly 30% lower void fractions than the stratified cases. Although the observation that non-uniform distribution of bubbles in the incoming plane would cause an uneven distribution of downstream void fraction is intuitive, the corresponding increase in the total void fraction is not. One speculation is that the stratified random distributions may cause some bias which resulted in more bubbles to be entrained into the tip vortices than the uniform distribution.


Figure 10. Comparison of time-averaged void fractions vs. distance x for different initial nuclei distributions.

Since the main contribution to the increase in void fraction comes from bubbles entering cavitating regions, we can study the number of bubbles which encounter these zones for these three cases. From previous work [15],[18] we know that only the nuclei which pass through a "window of opportunity" upstream of the propeller will be entrapped in the tip vortex and cavitate. In order to determine this "window" a total of 900 bubbles were released from a 30×30 grid array in a 2D r-θ plane. Each bubble is then tracked and the minimum pressure it encounters during its course is recorded. These recorded values are then plotted to obtain pressure contours which can be used to determine if a bubble release in the upstream plane will cavitate or not. Figure 11 shows this "window of opportunity" for bubbles of radii R_{in} = 200 μm. (Note that the window of opportunity is also a function of bubble radius.) Since the pressure coefficient can be related to the cavitation inception number i.e. $c_{pmin} \simeq -\sigma_i$, nuclei in the regions of $C_{pmin} < -2.75$ will tend to grow explosively. On comparing the three upstream bubble distributions for this "window of opportunity" we find that only 11% of the R_{in} = 200 μm bubbles in the uniform distribution pass this "window of opportunity", while for both

the stratification cases this number is around 14%. Hence increasing the probability of getting captured in the "window of opportunity" causes an increase in the void fraction downstream. This is probably due to effectively placing more bubbles in the upper region of domain, i.e. closer to the propeller tip.
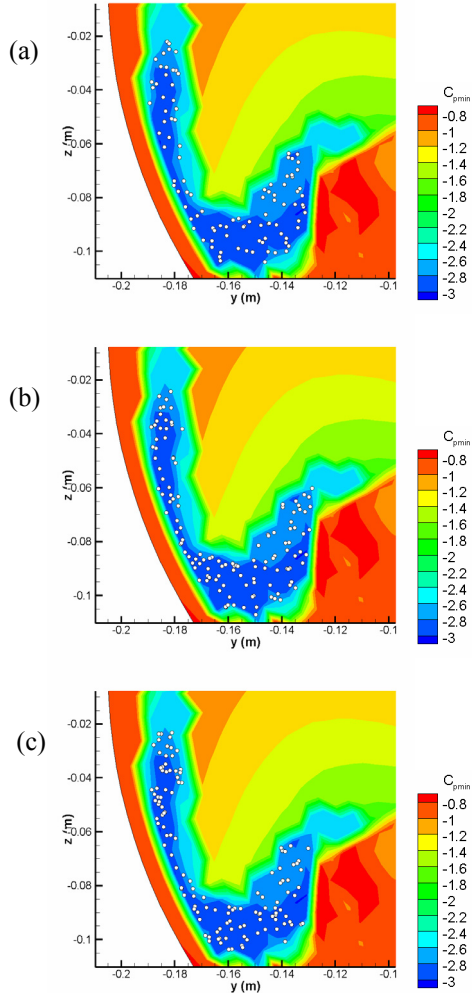
Figure 11. "Window of opportunity" for R_{in} = 200 μm and the corresponding bubbles in this window for (a) uniform distribution and stratified distribution in (b) 1D and (c) 0.75D.
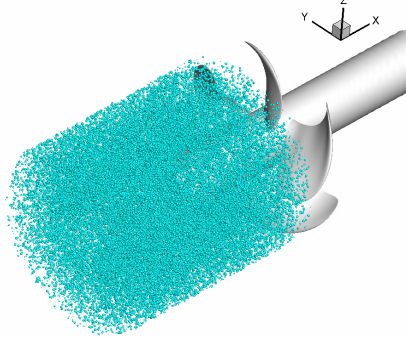
**Figure 12.** Upstream bubble release for investigating the effects of gravity.
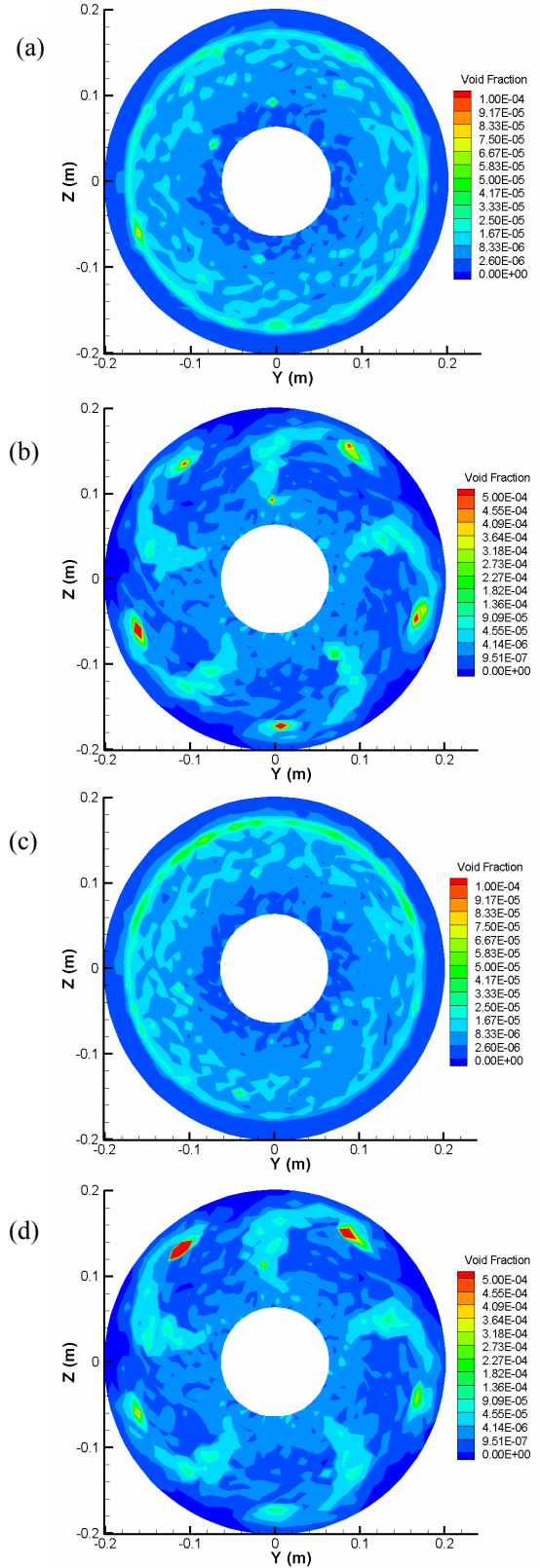
Figure 13. (a)&(c) Time-averaged and (b)&(d) phase-averaged void fractions at x=0.22 m for (a)&(b) without gravity and (c)&(d) with gravity cases respectively.

Effect of Gravity

In order to include non-uniform flow fields and the effect of gravity, computations cannot be conducted in a rotating frame and under the assumption of periodicity in the five blade passages. For this reason the bubbles are released in all the blade passages simultaneously as seen in Figure 12. Due to increased computational effort required to simulate all the five passages simultaneously only RANS solution was considered so far. The advance coefficient was $J = 1.1$ and the cavitation number $\sigma = 1.75$. A uniform bubble size of $R_{in} = 100$ μm was used to demonstrate the effect of gravity.

Figure 13 shows both the time-averaged and the phase-average void fractions at x=0.22 m for the cases with and without gravity. It is seen that when accounting for gravity effects higher void fractions are computed in the upper region of the flow. One can see this difference more clearly via the phase average void fractions in this plane. The presence of gravity causes the bubbles to migrate towards the top causing a difference in the distribution of void fractions between the various tip vortices. However, it is our observation that the integrated time-averaged values along the x-direction did not change between these two cases. This may be due to the small scale of the propeller. The validity of this speculation will be tested in the future at several propeller scales and with the proper use of DNSS solutions.
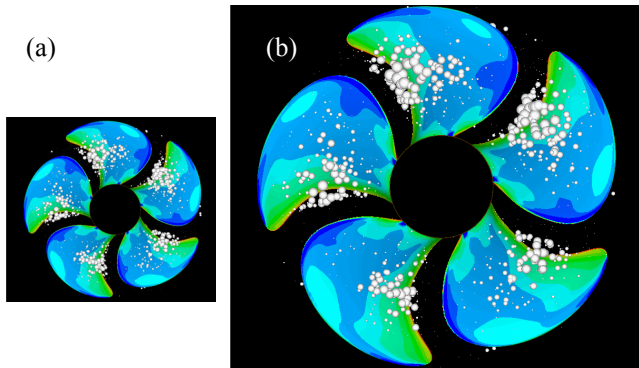

Figure 14. Comparison of cavitation bubbles appearance on the propeller blade surfaces for (a) small scale, 0.4m and (b) larger scale, 0.8m.

Effect of Propeller Scale on the Results

The above results were for a propeller diameter $D = 0.4$ m. To study the effect of propeller size on the bubble modification downstream we have conducted the same computations for a propeller having twice that diameter: $D = 0.8$ m. To conserve the advance coefficient at J=1.1 the rotational speed was changed to $n = 725$ rpm. The rest of the parameters including the bubble size and initial void fraction were kept the same. Figure 14 shows comparison of the cavitation bubbles appearance on the propeller blade surfaces between the small and the large scale. It is seen that, as the propeller size increases, the difference in cavitation appearance between the

upper blades and the lower blade surface becomes more significant. The time and phase-averaged void fractions for the large scale are shown in Figure 15. By comparing the results to those of Figure 13, one can see that gravity effects on the void fraction distribution downstream are augmented as the scale is increased.
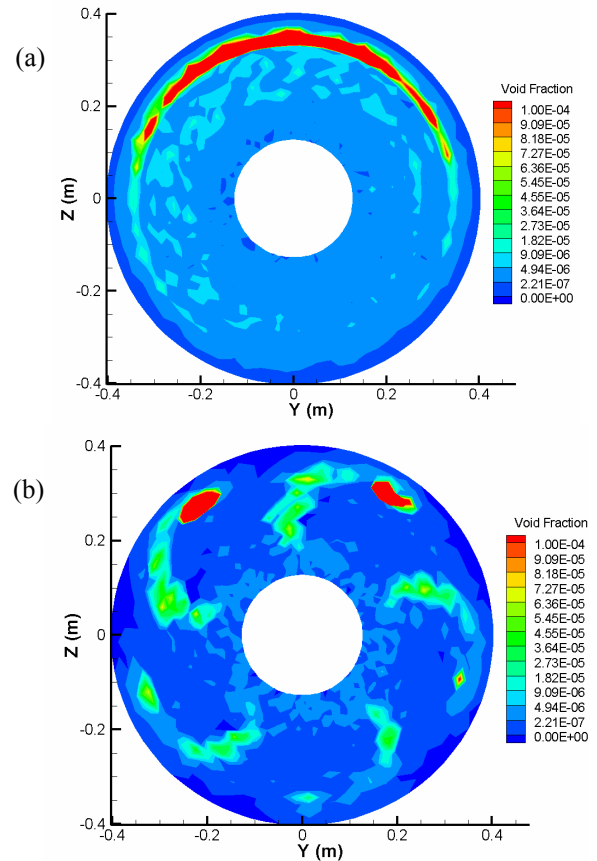
Figure 15. Large scale (a) time-averaged and (b) phase-averaged void fractions in the x=0.26 m plane.
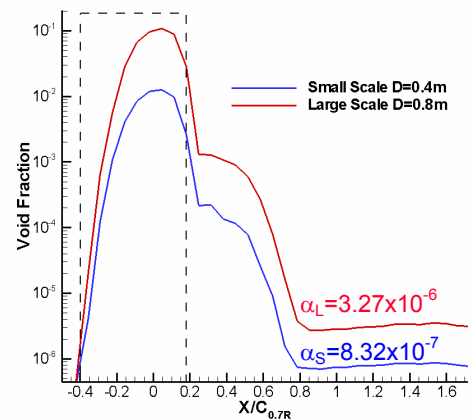
Figure 16. Comparison of time-averaged void fraction for the two scales along x.

To obtain a more quantitative comparison between these two scales, we compare the variations of the time-averaged void fraction for the two cases along x as shown in Figure 16. It can be seen that downstream of the propeller, the void fraction for the larger scale is, $\alpha_L = 3.27 \times 10^{-6}$ while for the smaller scale it is, $\alpha_S = 8.32 \times 10^{-7}$. Hence the void fraction scale ratio is approximately $\alpha_L / \alpha_S = 4$ which is the square of the scale ratio, $D_L / D_S = 2$.

CONCLUSIONS

The influence of the presence of a rotating propeller on the process of bubble entrainment was studied numerically. The flow field around a propeller was computed first using a RANS approach and then improved using matched DNSS simulations. The computations showed that the void fraction was significantly increased downstream of the propeller with use of the more accurate DNSS solution. The DNSS solution leads to a wider and larger bubble size distribution downstream as compared to the RANS.

The effect of advance coefficient was also explored. Change in the advance coefficient was found to cause a change in the cavitation appearance and location as well as in the downstream void fraction distribution.

Stratification in the nuclei distribution upstream of the propeller was found to cause stratified void fraction distribution downstream and higher void fractions. This was found to be due to more number of bubbles passing through the "window of opportunity" when the bubbles were stratified. This contributes to an increase in the explosive growth and collapse of the bubbles.

The effects of gravity and propeller size on the nuclei population modification were also preliminarily investigated using modeling of the full propeller domain but only with RANS. Gravity was seen to lead to an uneven spatial distribution of the void fractions downstream biased towards the top. Increasing the propeller size leads to an increase in the void fraction downstream of the propeller. Preliminary calculations indicate that the void fraction increase downstream of the propeller scales with the square of the size ratio.

ACKNOWLEDGMENTS

NOMENCLATURE

α = Void fraction
β_c = Artificial compressibility factor
C = Dissolved gas concentration
$C_{0.7R}$ = Propeller chord length at 0.7 radius section

C_D = Drag coefficient
C_L = Lift coefficient
C_{pmin} = Coefficient of pressure
C_S = Dissolved gas concentration
D = Propeller diameter
D_g = Molar diffusivity of gas
H = Henry's constant
$J = U_\infty / nD$ = Advance Coefficient
μ = Dynamic viscosity
ν = Kinematic viscosity
n = Propeller rotational speed
$\dot{n}_g$ = Transfer rate of gas moles
Ω = Angular velocity
$\boldsymbol{\omega}$ = Vorticity
p = Pressure
p_{enc} = Surface averaged bubble encountered pressure
p_g = Gas pressure
ρ = Liquid density
ρ_b = Bubble density
$\mathbf{r}$ = Radial position vector
$R(t)$ = Bubble radius
R_{in} = Initial bubble radius
$R_e = \sqrt{U_\infty^2 + \left(0.7\pi nD\right)^2} \cdot C_{0.7R}/\nu$ = Reynolds Number
σ = Cavitation number
T = Temperature
$\mathbf{u} = (u, v, w)$ = Flow Velocity
$\mathbf{u}_b$ = Bubble velocity
$\mathbf{u}_{enc}$ = Surface averaged bubble encountered velocity
U_∞ = Freestream (inflow) velocity
V = Volume

Subscripts
b = bubble properties
g = gas conditions
L = Large scale
S = Small scale
v = vapor conditions

REFERENCES

[1] Paterson, E.G., Hyman, M, Stern, F., Carrica, P.M., Bonetto, F., Drew, D.A., Lahey, R.T. Jr., "Near and Far-Field CFD for a Naval Combatant Including Thermal-Stratification and Two-Fluid Modeling," 21st Symposium on Naval Hydrodynamics, Trondheim, Norway, 1996.

[2] Carrica, P.M., Bonetto, F., Drew, D.A., Lahey, R.T. Jr., "A polydisperse Model for Bubbly Two-Phase Flow around a Surface Ship," International Journal of Multiphase Flow, Vol. 25, 1999, pp. 257-305.

[3] Waniewski, T.A., Brennen, C.E., "Measurement of Air Entrainment by Bow Waves," ASME Journal of Fluids Engineering, Vol. 123, 2000, pp. 57-63.

[4] Hsiao, C.-T., Jain, A. Chahine, G.L., "Effect of Gas Diffusion on Bubble Entrainment and Dynamics around a Propeller." 26th Symposium on Naval Hydrodynamics, Rome, Italy, 17-22, Sept. 2006.

[5] Dacles-Mariani, J., Zilliac, G.G., Chow, J.S., Bradshaw, P., "Numerical/Experimental Study of a Wingtip Vortex in the Near Field," AIAA Journal, **33**, No. 9, 1995, pp.1561-1568.

[6] Hsiao, C.-T., Pauley, L. L. "Numerical Study of the Steady-State Tip Vortex Flow over a Finite-Span Hydrofoil", Journal of Fluids Engineering, **120**, pp. 345-353, 1998.

[7] Hsiao, C.-T., Pauley, L. L. "Numerical Computation of the Tip Vortex Flow Generated by a Marine Propeller", Journal of Fluids Engineering, **121**, No.3, pp. 638-645, 1999.

[8] Hsiao, C.-T.. Chahine, G.L., "Numerical Study of Cavitation Inception Due to Vortex/Vortex Interaction in a Ducted Propulsor." SNAME Journal of Ship Research, **52**, Number 2, pp. 114-123, June 2008.

[9] Hsiao, C.-T., Chahine, G.L., "Scaling of Tip Vortex Cavitation Inception for a Marine Open Propeller." 27th Symposium on Naval Hydrodynamics, Seoul, Korea, 5-10, Oct. 2008.

[10] Rogers, S. E., Kwak, D., Kiris, C., "Steady and Unsteady Solutions of the Incompressible Navier-Stokes Equations," AIAA Journal, **29**, No. 4, pp. 603-610, 1991.

[11] Chorin, A. J., "A Numerical Method for Solving Incompressible Viscous Flow Problems," Journal of Computational Physics, **2**, pp. 12-26, 1967.

[12] Roe, P. L., "Approximate Riemann Solvers, Parameter Vectors, and Difference Schemes," Journal of Computational Physics, **43**, pp. 357-372, 1981.

[13] Baldwin, B. S., Barth, T. J., "A One-Equation Turbulence Transport Model for High Reynolds Number Wall-Bounded Flows," NASA TM 102847, 1990.

[14] Johnson, V.E. and Hsieh, T., "The Influence of the Trajectories of Gas Nuclei on Cavitation Inception," Sixth Symposium on Naval Hydrodynamics, pp. 163-179, 1966.

[15] Hsiao, C.-T., Chahine, G. L., Liu, H.-L., "Scaling Effects on Prediction of Cavitation Inception in a Line Vortex Flow", Journal of Fluid Engineering, **125**, pp.53-60, 2003.

[16] Gilmore, F. R., "The growth and collapse of a spherical bubble in a viscous compressible liquid," California Institute of Technology, Hydro. Lab. Rep. 26-4, 1952.

[17] Haberman, W.L., Morton, R.K., "An Experimental Investigation of the Drag and Shape of Air Bubbles Rising in Various Liquids," Report 802, DTMB, 1953.

[18] Hsiao, C.-T., Chahine, G. L., "Prediction of Vortex Cavitation Inception using Coupled Spherical and Non-Spherical Models and Navier-Stokes Computations", Journal of Marine Science and Technology, **125**, No. 3, pp.99-108, 2004.

[19] Plesset, M.S., Zwick, S.A., "A Non-steady Heat Diffusion Problem with Spherical Symmetry," Journal of Applied Physics, **23**, No.1, pp. 95-98, 1952.

[20] Chahine G.L., Kalumuck K.M., "The Influence of Gas Diffusion on the Growth of a Bubble Cloud", ASME Cavitation and Multiphase Flow Forum, Cincinnati, Ohio, **50**, pp. 17-21,1987.

[21] Chahine G.L., Kalumuck K.M., Perdue, T. , "Cloud Cavitation and Collective Bubble Dynamics," ONR Contract N00014-83-C-0244 Final Report. Tracor Hydronautics Technical Report 83017-1, March 1986.